RESEARCH ARTICLE

Effects of austenitizing temperature on the microstructure and electrochemical behavior of a martensitic stainless steel

Si-Yuan Lu · Ke-Fu Yao · Yun-Bo Chen · Miao-Hui Wang · Yang Shao · Xue-Yuan Ge

Abstract The aim of this work is to study the effects of austenitizing temperatures on the microstructure and electrochemical properties of a typical type of martensitic stainless steel (MSS) in 3.5 wt% NaCl aqueous solution. The microstructures of the experimental MSSs in different heat treatment states, such as annealed and quenched after different austenitizing temperatures, were characterized using SEM–EDS and XRD analysis. Electrochemical techniques, including potentiodynamic polarization and electrochemical impedance spectroscopy were also used to analyze the electrochemical behavior of the studied material in 3.5 wt% NaCl aqueous solution. The results show that the Cr-rich $M_{23}C_6$ carbides were precipitated during annealing, and then dissolved into the steel matrix during austenitization. An increase in the austenitizing temperature can reduce the amount of Cr-rich $M_{23}C_6$ carbides in the quenched steels, improving the homogeneity of Cr distribution. The pitting potential of the quenched samples increased with the austenitizing temperature, and the passive films that formed on the samples austenitized at higher temperatures were more protective against chloride corrosion.

Keywords Martensitic stainless steel · Carbides · Potentiodynamic polarization · Electrochemical impedance spectroscopy · Pitting corrosion

S.-Y. Lu · K.-F. Yao (✉) · Y. Shao
School of Materials Science and Engineering, Tsinghua University, Beijing 100084, China
e-mail: kfyao@tsinghua.edu.cn

S.-Y. Lu
e-mail: lusiyuan11@mails.tsinghua.edu.cn

S.-Y. Lu · Y.-B. Chen (✉) · M.-H. Wang · X.-Y. Ge
State Key Lab of Advanced Forming Technology and Equipment, Advanced Manufacture Technology Center, China Academy of Machinery Science & Technology, Beijing 100083, China
e-mail: webmaster@ht.org.cn

1 Introduction

Owing to the combined attack of the chloride and acids released during the decomposition of thermoplastics (such as PVC) via overheating [1], the working environments for plastic injection molding are extremely hostile. To extend the working life of plastic injection molds, stainless steels, especially the 13 wt% Cr-type martensitic stainless steels, are more often used as "corrosion resistant plastic mold steel" in plastic mold production. However, such 13 %Cr-type martensitic stainless steels are sensitive to localized corrosion, especially pitting corrosion, in certain Cl^- containing environments [2, 3]. In these cases, chloride acts as a depolarizer, breaking the passive layer, and the metal cations exhibit considerable solubility in chloride solutions [4], resulting in the occurrence of pitting corrosion due to the passive film breakdown [5, 6]. Subsequently, the working life of the molds would be reduced and appearance of the plastic products can be damaged. Hence, it is important to enhance the anti-corrosion properties of the mold steels.

Almost all martensitic stainless steel must undergo quenching and tempering process before use to achieve better mirror surface property and corrosion, abrasion, and wear resistance [7, 8]. Generally, the austenitizing temperature mainly affects the microstructure of martensitic steel by strongly influencing the distribution of insoluble

carbides and retained austenite in the steel's matrix. Pits always initiate at some chemical or physical heterogeneity in the metal surface, such as inclusions, second phase particles, and solute-segregated grain boundaries [2, 9]. Once a pit initiates, it is always accompanied by the breakdown and repassivation of passive films on metal surface. A metastable pit can become stable pitting [10], which continuously induces the depassivation of the stainless steel, leading to severe corrosion. In addition, the localized enrichment of Cr caused by Cr-rich carbides would create a Cr-depleted zone in the steel matrix [11, 12] that degrades its corrosion resistance. Therefore, the insolvable carbides in stainless steels' matrix under different austenitizing temperatures would affect the corrosion performance of stainless steel, either in terms of the initial pitting sites or localized Cr enrichment. However, the effects of microstructures containing carbides on the pitting resistance of the corrosion-resistant plastic mold steels have not been sufficiently studied [13, 14], and understanding them would facilitate the development of durable, high-performance plastic mold steels.

In this study, the microstructures and the electrochemical properties of a typical corrosion-resistant plastic mold steel that annealed and quenched after austenitizing at different temperatures are examined. The results indicate that the microstructures and the electrochemical properties of the MSS are quite different, and the related mechanisms are discussed.

2 Experimental

2.1 Material and heat treatment

The corrosion-resistant plastic mold steel used in present work was 13 %Cr-type martensitic stainless steel (MSS), which has the basic chemical composition (in wt%) of 0.38C, 0.60Mn, 0.90Si, 13.60Cr, 0.30V, and balance Fe. Before austenitizing, the MSSs were annealed at 850 °C for 12 h and cooled to 700 °C in a furnace for 4 h, followed by air cooling. After annealing, they were, respectively, austenitized at 980, 1030, 1080, and 1130 °C for 45 min, followed by oil quenching (OQ). The samples prepared using the aforementioned heat treatments were marked based on their heat treatment procedure, respectively. For instance, the sample of annealed steel was denoted as an "annealed sample," while one austenitized at 980 °C was denoted as a 980 sample, hereafter.

2.2 Microstructure observation and carbides analysis

X-ray diffraction (XRD) analyses of the annealed and quenched samples were carried out on a Rigaku/SMART Lab X-ray diffractometer, with Cu Kα radiation. Continuous mode with a scan rate of 6°/min and 2θ ranging from 40° to 90° was applied to analyze the main structure of each specimen, while the step mode with a 0.01° step size, 2 s step time, and 47°–52° of 2θ range were used to gather the detailed information on the structure for each heat-treated specimen.

Microstructure of each heat-treated specimen was observed using field emission scanning electron microscopy (FE-SEM) of type LEO-1530. All of the specimens were ground, mechanically polished, and then etched using a particular etchant comprising 25 ml HNO_3, 25 ml HCl, and 50 ml distilled water. The distribution of Cr and the chemical composition of carbides in each specimen were examined with an Oxford Instruments energy dispersive spectrometer (EDS) installed on the FE-SEM.

2.3 Electrochemical measurements

A 3-mm-thick plate was cut from a $\phi10$ mm MSS rod, and then mounted in epoxy resin, leaving an exposed area around 0.7854 cm^2. The samples were ground successively with 400-, 800-, and 1,200-grit SiC papers to obtain a fine surface. The 3.5 % NaCl aqueous solution was prepared by dissolving analytically pure NaCl in 18.25 MΩ cm deionised water as the corrosion medium (pH 5.6–5.8).

The electrochemical measurements were carried out using a CS350-type electrochemical workstation (Corrtest Instrument, China) with a three-electrode cell, which comprised a thin platinum plate as counter electrode (CE), a saturated calomel electrode (SCE) as reference electrode (RE), and the sample prepared using the above method as the working electrode (WE). Strong cathodic polarization at −500 mV (vs. SCE) was firstly conducted for 0.5 h to remove the initial passive film from the surfaces of the WEs. Before the EIS and polarization measurements were taken, the open circuit potentials (OCPs) of all WEs were monitored for 0.5 h, until a stable OCP was achieved.

After a stable OCP was acquired, the EIS measurements were performed with a ±10 mV (vs. OCP) amplitude perturbation and a frequency range from 10^{-2} to 10^5 Hz (i.e., 10, 7.94, 6.31, 5.01…1 Hz) and the results were fitted and analyzed by Zview.

The polarization potential was scanned at 0.166 mV s^{-1} (vs. SCE) from −500 mV (vs. OCP) in room temperature (23–26 °C) to eliminate the uncertainty of original passive film, and was terminated until the current density of the sample surface reaching 0.1 mA cm^{-2}, where the corresponding potential is defined as the breakdown or pitting potential (E_{pit}) of passive films [2]. The electrochemical results of each type sample were averaged based on at least three parallel specimens from the same heat treatment plot.

3 Results and discussion

3.1 Microstructure and precipitates

Surface hardness measurements of experimental steels reveal that the hardness value of annealed sample is 21.3 HRC, which is much lower than that of quenched samples (>56 HRC, see in supplementary materials). Figure 1 shows the XRD spectra of specimens that were annealed and quenched after different austenitizing temperatures. The peaks of the α phase with a BCC structure are presented in all of the samples. However, the axial ratio of martensite and ferrite is so close (10^{-4}–10^{-5} nm) [15, 16] that the separate peaks of these two phases cannot be detected merely by XRD analysis. According to the surface hardness measurements, the hardness value recorded for the annealed sample is 21.3 HRC, and those of the quenched samples are all higher than 56 HRC. Thus, the α phase detected by XRD in experimental samples can be further indexed as ferrite in annealed sample, and martensite in quenched samples. In addition, with the increase in austenitizing temperature, the γ phase is present in the 1,080 and 1,130 samples (Fig. 1a, b), which can be considered as retained austenite. This may be attributed to the high stability of austenite promoted by the high C content that results from the dissolution of $M_{23}C_6$ carbides at high austenitizing temperatures [17, 18].

The XRD spectra in Fig. 1b show the weak peaks within the 2θ range of 47°–52° for the annealed and quenched samples. The diffraction angles fitted by MDI Jade version 5.0 fitting software were 48.514(4)°, 50.881(4)°, and 51.659(5)° for annealed sample; 48.411(20)° and 50.799(30)° for 980 sample, and 48.497(20)°, 50.738(28)° for 1,030 sample—indexed as the different peaks of (440), (531), and (600) plane for Cr-rich $M_{23}C_6$, respectively.

Fitting results reveal that the lattice parameter of Cr-rich $M_{23}C_6$ (FCC) in annealed, 980 and 1,030 samples are 1.061(1), 1.063(1), and 1.064(1) nm, respectively. Based on the measurement precision of the present experiments, the obtained lattice parameters can be regarded as the same, however, they are slightly smaller than the value of 1.0658(1) nm of pure $Cr_{23}C_6$ noted in Erdos's research [19], perhaps due to the solution of Fe into the pure $Cr_{23}C_6$ [20]. In addition, the peak intensity of Cr-rich $M_{23}C_6$ of the annealed sample was much greater than that of the quenched samples. As the austenitizing temperature increased from 980 to 1,030 °C, the peak intensity of Cr-rich $M_{23}C_6$ decreased; when austenitizing temperature exceeded 1,080 °C, the peaks of Cr-rich $M_{23}C_6$ disappeared and the peak of γ(200) was observable. It turned out that the Cr-rich $M_{23}C_6$ initially precipitated during annealing, then started to dissolve during austenitizing and with the tendency of thoroughly dissolved in steel matrix as the austenitizing temperature increase. Thus, the $M_{23}C_6$ carbides existed in 980 and 1,030 samples could be reasonably recognized as "undissolved $M_{23}C_6$ carbides".

The microstructures of the annealed sample shown in Fig. 2a, b included ferrite + $M_{23}C_6$ without pearlite, which might be attributable to the reduction of carbon in steel matrix when carbon has dissolved into carbides, in accordance with other reports [21], while martensitic laths could be observed in the quenched samples (Fig. 2c, d, e, and f). There were more carbides in the annealed sample than in the quenched samples. The amount of carbides decreased as the austenitizing temperature increased, such that when it reached 1,130 °C, no carbides could be observed. As was confirmed by XRD analysis, the main carbides observed in annealed, 980 and 1,030 samples are Cr-rich $M_{23}C_6$-type, which exhibit as some round or elongated particles with a size range of 1–2 μm and smooth edges (Fig. 2a, b, c, and d). They were typically noted between the grain boundary and within the martensitic lath, indicating that they precipitated during annealing, and tended to dissolve more in the steel matrix as austenitizing temperature increased.
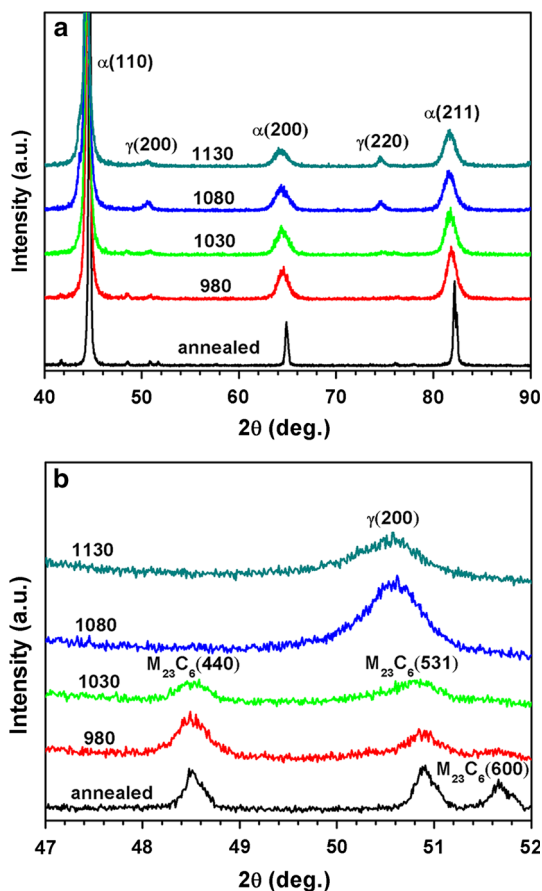
Fig. 1 XRD profiles of the samples after different heat treatments: **a** diffraction angles from 40° to 90° and **b** detail information between diffraction angles from 47° to 52°
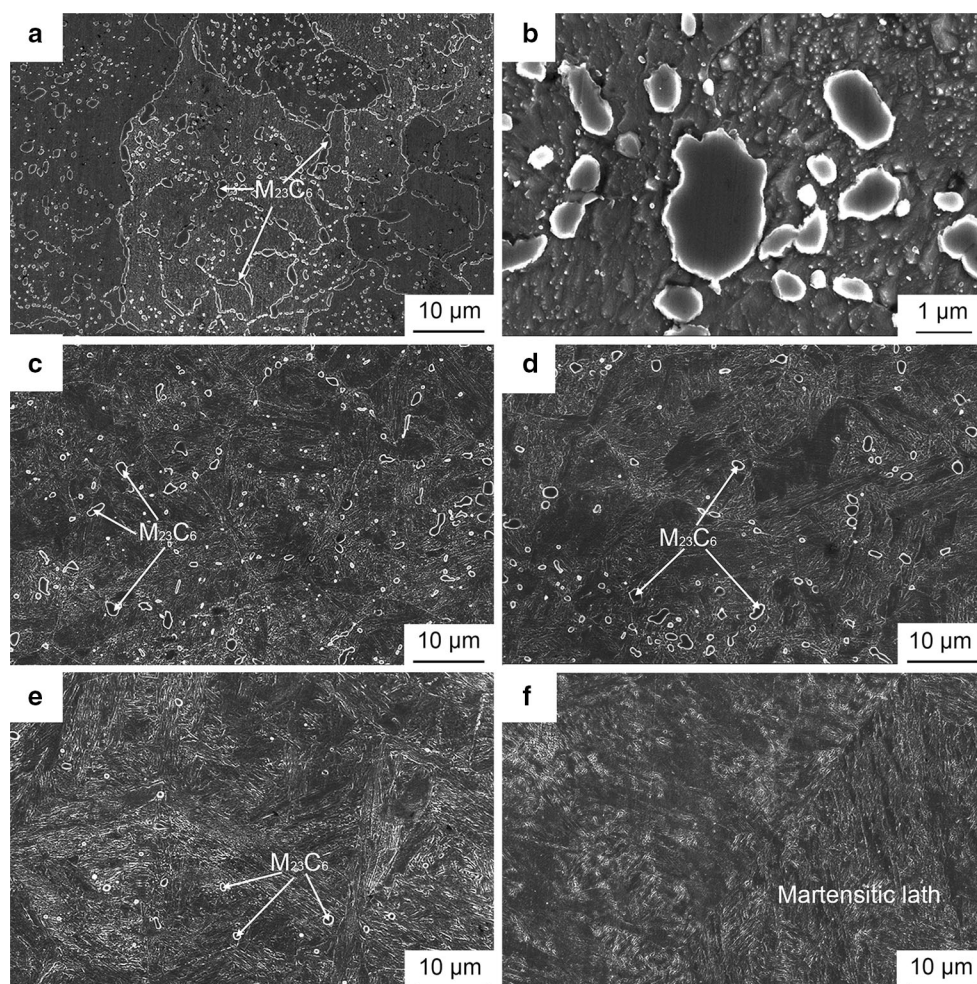
Fig. 2 SEM morphology of **a** annealed sample, **b** local magnification of carbides in (**a**), and quenched samples after austenitization at **c** 980 °C, **d** 1,030 °C, **e** 1,080 °C, and **f** 1,130 °C

When the austenitizing temperature reached a critical value (1,130 °C for instance), the Cr-rich $M_{23}C_6$ would be totally dissolved in the austenite phase of the steel, and did not precipitate during quenching.

3.2 Carbides characterization

Following the literature [13, 22, 23], the preferable austenitizing temperature for 13 wt%Cr-type stainless steel is in the range of 1,020–1,050 °C, and the undissolved $M_{23}C_6$ has been proven to gain the same structure parameter after 980 and 1,030 °C austenitization. Therefore, the 1,030 sample was selected here for further study of Cr-rich $M_{23}C_6$. The annealed and 1,130 samples were also selected for comparison. The distribution maps for the elements Cr and Fe using energy dispersive spectrometer (EDS) in the annealed, 1,030 and 1,130 samples are shown in Fig. 3. Clearly, the distributions of Cr and Fe in the annealed and 1,030 sample are non-uniform, whereas in the

1,130 sample they were uniform. Compared with the microstructure morphologies and distribution maps, the Cr-rich regimes in the annealed and 1,030 samples were $M_{23}C_6$ combined with a relative depleted zone of Fe element.

The composition analysis of the selected micro regions (clearly marked by A, B, C, D, E, F, and G in Fig. 3) was conducted via SEM–EDS. In Fig. 3, points A and B (D and E) represent the $M_{23}C_6$ carbides in annealed (1,030) sample, and points C, F, and G can be recognized as the matrix of all three samples, respectively. The results are shown in Table 1. However, carbon cannot be detected due to its low content in steel and the limited detection accuracy of the spectrometer when applied to such a light element. The Cr content (in weight %) of $M_{23}C_6$ in both the annealed and 1,030 samples was around 48 %, which was higher than that in the matrix (around 13 %). In addition, the Cr content in the matrix of 1,130 samples was similar to that of other samples. However, the Cr distributions seemed to be
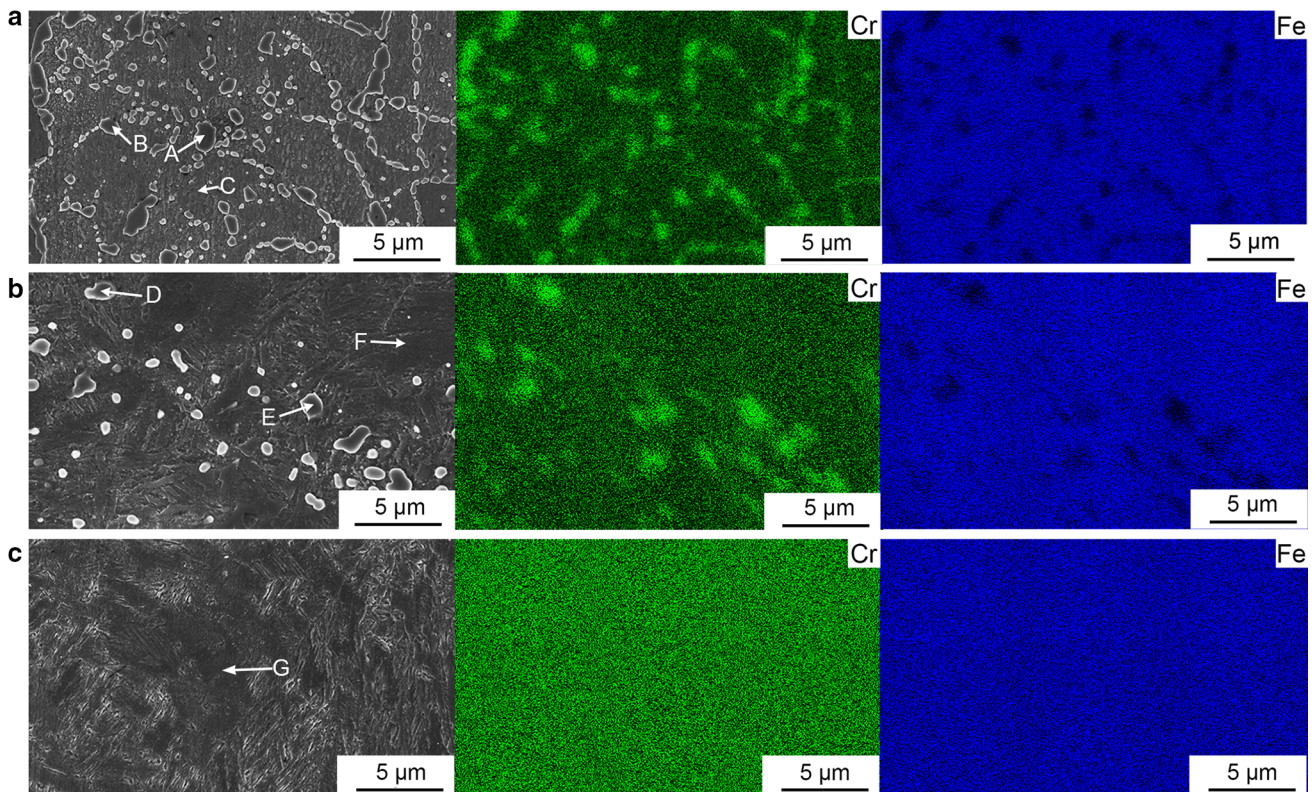
Fig. 3 Element distribution maps (mainly of Cr and Fe) via EDS of the micro zone of experimental MSSs: **a** annealed sample, **b** 1,030 sample, and **c** 1,130 sample

Table 1 Results of composition analysis via EDS (corresponding to the points in Fig. 3)

| Points	Chemical composition (in wt%)				
	Fe	Cr	Mn	Si	V
A	49.88	47.19	1.80	0.37	0.76
B	48.25	48.89	1.64	0.44	0.78
C	84.26	13.20	1.04	1.07	0.33
D	47.46	47.07	1.55	0.29	1.33
E	48.07	48.69	1.60	0.27	1.05
F	84.31	13.30	1.00	0.92	0.27
G	83.42	13.42	1.05	1.07	0.25

irrelevant to the precipitating location, as the Cr content of $M_{23}C_6$ precipitated among the grain boundary and martensitic laths are almost the same. Furthermore, the silicon (Si) content in $M_{23}C_6$ is significantly lower than that in matrix, confirming that Si is not a carbide-forming element.

As reported, the $M_{23}C_6$ is always the first phase formed in austenitic stainless steel and some other low-carbon high alloying steels during annealing, usually precipitating at the grain boundary (GBs) due to high interfacial energy [24, 25]. With higher Cr content and relatively lower Fe,

the precipitation of $M_{23}C_6$ creates a lack of Cr among the steel matrix, becoming preferential sites for pitting corrosion [26]. However, as was shown in Fig. 3a, the bright contrast of Cr in $M_{23}C_6$ particles indicates a localized enrichment of Cr. The analysis of Cr content distribution through line scanning (see in supplementary materials) across the carbide particles further confirmed that the Cr content gradually increased from the matrix to the carbides, indicating Cr enrichment in the carbide area. However, no Cr-depletion area was found around $M_{23}C_6$, confirming that Cr-rich $M_{23}C_6$ carbides dissolved before quenching.
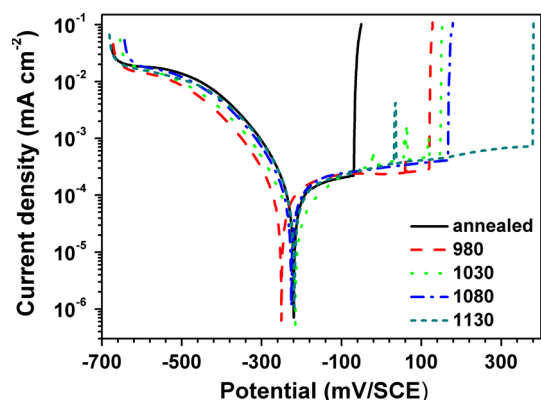
3.3 Electrochemical performance

Figure 4 illustrates the variation of the open circuit potential (OCP) of experimental stainless that were annealed and quenched in different austenitizing temperatures in the 3.5 wt% NaCl aqueous solution. In all cases, the shapes of the curves are similar, during the first 600 s of immersion, OCP increased dramatically with time and then reached a stationary state. The values of OCP increased with the austenitizing temperature, and some potential transients were observed. Figure 5 shows the potentiodynamic polarization curves of experimental martensitic stainless steels after different heat treatments. The distribution of
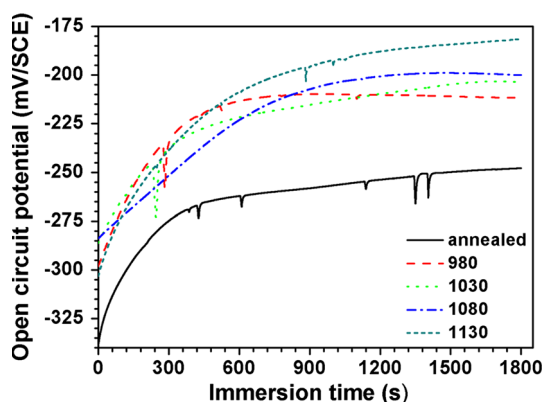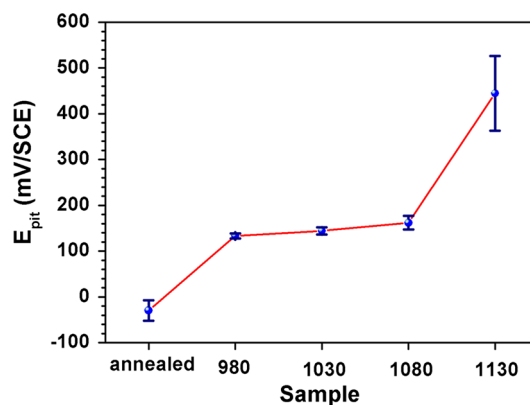
Fig. 4 The open circuit potential (OCP) of experimental steels in 3.5 wt% NaCl aqueous solution after 0.5 h-long cathodic polarization at −500 mV (vs. SCE) around 25 °C

Fig. 6 Pitting potential of experimental stainless steels based on potentiodynamic polarization curves

experimental steels' pitting potentials, as obtained from the potentiodynamic polarization curves, is shown in Fig. 6. According to Fig. 5, all of the samples exhibited a clear passive region and a sharp increase in current density after the breakdown of passive film in 3.5 wt% NaCl aqueous solution. Several current transients were observed in passive region, especially from the polarization curves of the annealed, 980 and 1,030 samples, which may be related to the nucleation and repassivation of metastable pits of stainless steels that occurred at such active sites as carbides [10, 27]. Figure 6 reveals that the E_{pit} of the annealed sample (−30 mV) was much lower than that of the quenched samples, and E_{pit} increased with the austenitizing temperature; specifically, when austenitizing temperature reached 1,130 °C, the E_{pit} of experimental steel increased to 400 mV, which was much higher than that of other samples austenitized at lower temperature (128–178 mV), this indicates that the pitting resistance of the quenched samples was better than annealed sample, and an increase

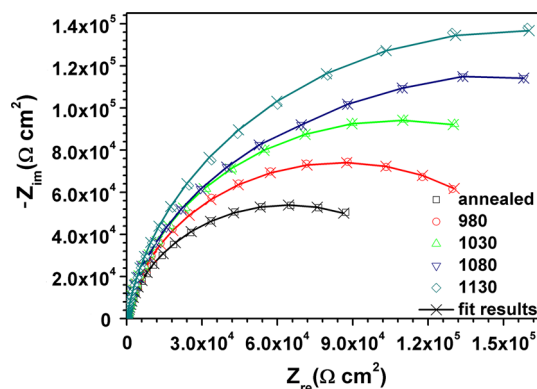in austenitizing temperature can enhance the resistance of quenched martensitic stainless steels to pitting corrosion.

Figure 7 shows the Nyquist plots of the experimental steels at OCP under the same experimental condition as the potentiodynamic polarization. It can be seen that the EIS spectra of all the samples exhibited a single capacitive in the high-medium frequency range, which is associated with the double layer capacitance (C_{dl}) and passive layer capacitance (C_{film}) in parallel with the charge transfer resistance. However, since the C_{film} of MSS is much lower than C_{dl}, the total capacitance here is mainly depended on the passive film other than the double electric layer [28–30]. As is shown in Fig. 7, the diameter of the arc of the annealed sample was smaller than that in the quenched samples, and the diameter increased with the austenitizing temperature, indicating that the surface of the quenched samples that austenitized at higher temperatures could form more protective and well-structured passive films due to the improved homogeneity of local areas from reducing the

Fig. 5 Potentialdynamic polarization curves of experimental stainless steels in 3.5 wt% NaCl at room temperature (around 25 °C)

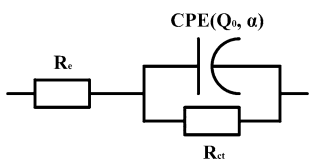**Fig. 7** EIS spectra of experimental steels in 3.5 wt% NaCl (aq) at OCP

Fig. 8 Equivalent circuits used to fit the experimental impedance data

amount of Cr-rich carbides, increasing the corrosion resistance of the martensitic stainless steel in Cl⁻ containing solution.

El-Egamy and Badaway [31] proposed an equivalent circuit model to simulate the behavior of 304 stainless steel in a sodium sulphate solution. This model can be used to fit the electrochemical performance of the present experimental samples. The equivalent circuit is shown in Fig. 8, in which the parallel-connected elements (CPE//R_{ct}) are used to describe the electrochemical process at the substrate/passive film interface.

The impedance of CPE can be described by:

$$Z(CPE) = Q_0^{-1}(j\omega)^{-\alpha}, \tag{1}$$

where Q_0 is the CPE parameters, j is $\sqrt{-1}$, ω is angular frequency and α is the dispersion coefficient related to surface inhomogeneity. The impedance resistance of the electrode/passive film/solution system can be calculated by:

$$Z = Z(R_e) + Z(R_p//CPE) = R_e + \left[R_{ct}^{-1} + Q_0(j\omega)^{\alpha}\right]^{-1}, \tag{2}$$

where CPE is the constant-phase element, and reflects a distribution of reactivity of passive films, R_{ct} the charge transfer resistance, and R_e the Ohmic or solution resistance [32, 33]. Table 2 gives the best fitting results of EIS based on the equivalent circuit model shown in Fig. 8.

From Table 2, the α values of quenched stainless steels are in the range of 0.91–0.92, which are higher than for the annealed sample (0.89), it implies that the electrochemical behavior of passive films is mildly deviated from a pure

capacitive behavior. When $\alpha < 1$, the system shows behavior that has been attributed to surface heterogeneity, and the CPE parameter Q cannot represent the capacitance. Some researchers have explored the relationship between CPE parameters and the interfacial capacitance, and their results have shown that the effective capacitance (C_{eff}) is proportional to $Q^{-\alpha}$. Additionally, Hirschorn [32] proposed that the thickness of oxide films formed on an Nb disk electrode in 0.1 M NH₄F solution increases as Q decreases. In our work, when the austenitizing temperature rose from 980 to 1,130 °C, the Q_0 values of the quenched samples decreased from 4.33×10^{-5} to 3.13×10^{-5} Ω^{-1} cm^{-2} s$^{\alpha}$, and the R_{ct} values increased from 1.72×10^5 to 3.13×10^5 Ω cm^2, indicating that the increase in corrosion resistance of passive films due to either film thickening or compositional modification was obtained by improving local homogeneity through increasing austenitizing temperature, which is well matched with the results of potentiodynamic polarization experiments.

According to the above analysis, although no poor Cr zone was observed around undissolved Cr-rich M₂₃C₆ particles, the enrichment of Cr around undissolved M₂₃C₆ particles was clearly detected. It can be inferred that the local areas with different Cr contents would possess different electrode potentials, and the enrichment of Cr in local areas around undissolved Cr-rich carbides would also induce depletion of Cr content in other areas. In addition, it is experimentally proved that the corrosion resistance of austenite is higher than ferrite/martensite, which is resulted from the fact that the austenite contains lower internal stresses and less defects [34, 35]. It is also reported that in duplex stainless ferrite is more chemically active than austenite and the metastable pits always preferentially initiate inside ferrite [36, 37]. Therefore, the retained austenite appeared in the steel matrix when the austenitizing temperature reached 1,080 °C could also enhance the pitting resistance of the MSSs quenched at higher austenitizing temperatures. As a result, reducing the amount of these Cr-rich carbides, which can be promoted by increasing the austenitizing temperature, should improve the corrosion resistance of MSSs.

Table 2 Fitted parameter values of experimental steels obtained from EIS spectra

Specimen	R_e/Ω cm² ± 0.6 %	CPE		R_{ct}/Ω cm² ± 5.2 %
		α(0–1) ± 0.3 %	$Q_0/(\Omega^{-1}$ cm^{-2} s$^{\alpha}) \pm 1.4$ %	
Annealed	3.26	0.89	5.97×10^{-5}	1.29×10^5
980	2.98	0.91	4.33×10^{-5}	1.72×10^5
1,030	2.98	0.91	4.06×10^{-5}	1.95×10^5
1,080	3.78	0.91	3.88×10^{-5}	2.29×10^5
1,130	3.74	0.92	3.13×10^{-5}	3.13×10^5

4 Conclusion

The Cr-rich $M_{23}C_6$ carbides observed in the MSSs matrix precipitated during annealing, and the increase in austenitizing temperature dramatically decreased the amount of unsolved Cr-rich $M_{23}C_6$ within the matrix of the MSS, especially when austenitizing temperature reached 1,130 °C, the $M_{23}C_6$ totally dissolved in the steel and did not precipitate again during quenching. It shows that in the sample quenched at 1,030 °C, there was a localized Cr enrichment area around the undissolved Cr-rich $M_{23}C_6$ carbides, whereas in the sample quenched at 1,130 °C, no Cr enrichment area could be found due to the disappearance of the Cr-rich $M_{23}C_6$ carbides. The present results indicate that the homogeneity of Cr distribution has been improved with the increase in austenitizing temperature.

Increasing the austenitizing temperature could enhance the corrosion resistance of the martensitic stainless steel to both pitting and general corrosion. The improvement in corrosion resistance of the steel was due to greater homogeneity in the distribution of Cr and a reduced amount of Cr-rich carbides. The polarization curve and EIS measurements confirmed that the decrease in $M_{23}C_6$ carbides content among the MSS matrix by increasing the austenitizing temperature allowed more protective and well-structural passive films to form, which enhanced the pitting corrosion resistance of martensitic stainless steel.

References

1. Shreir LL, Jarman RA, Burstein GT (1994) Corrosion control (Volume 2). Corrosion, vol 2. Butterworth-Heinemann, Oxford
2. Frankel G (1998) Pitting corrosion of metals a review of the critical factors. J Electrochem Soc 145(6):2186–2198
3. Ahmad S, Malik AU (2001) Corrosion behaviour of some stainless steels in chlorinated Gulf seawater. J Appl Electrochem 31(9):1009–1016
4. Sato N (1971) A theory for breakdown of anodic oxide films on metals. Electrochim Acta 16(10):1683–1692
5. Wang J, Su C, Szklarska-Smialowska Z (1988) Effects of Cl⁻ concentration and temperature on pitting of AISI 304 stainless steel. Corrosion 44(10):732–737
6. Nagarajan S, Karthega M, Rajendran N (2007) Pitting corrosion studies of super austenitic stainless steels in natural sea water using dynamic electrochemical impedance spectroscopy. J Appl Electrochem 37(2):195–201
7. Hill H, Raab U, Weber S, Theisen W, Wollmann M, Wagner L (2011) Influence of heat treatment on the performance characteristics of a plastic mold steel. Steel Res Int 82(11):1290–1296
8. Schneider R, Mesquita R (2011) IFHTSE Global 21: heat treatment and surface engineering in twenty-first century Part 16: advances in tool steels and their heat treatment Part 2-Hot work tool steels and plastic mould steels. Int Heat Treat Surf Eng 5(3):94–100
9. Williams DE, Newman RC, Song Q, Kelly RG (1991) Passivity breakdown and pitting corrosion of binary alloys. Nature 350:216–219
10. Pistorius PC, Burstein GT (1994) Aspects of the effects of electrolyte composition on the occurrence of metastable pitting on stainless steel. Corros Sci 36(3):525–538
11. Nakamichi H, Sato K, Miyata Y, Kimura M, Masamura K (2008) Quantitative analysis of Cr-depleted zone morphology in low carbon martensitic stainless steel using FE-(S) TEM. Corros Sci 50(2):309–315
12. Kaneko K, Fukunaga T, Yamada K, Nakada N, Kikuchi M, Saghi Z, Barnard JS, Midgley PA (2011) Formation of $M_{23}C_6$-type precipitates and chromium-depleted zones in austenite stainless steel. Scr Mater 65(6):509–512
13. Choi Y-S, Kim J-G, Park Y-S, Park J-Y (2007) Austenitizing treatment influence on the electrochemical corrosion behavior of 0.3 C-14Cr-3Mo martensitic stainless steel. Mater Lett 61(1):244–247
14. Marcelin S, Pébère N, Régnier S (2013) Electrochemical characterisation of a martensitic stainless steel in a neutral chloride solution. Electrochim Acta 87:32–40
15. Sun GF, Bhattacharya S, Dinda GP, Dasgupta A, Mazumder J (2011) Influence of processing parameters on lattice parameters in laser deposited tool alloy steel. Mater Sci Eng A 528(15):5141–5145
16. Rammo NN, Abdulah OG (2006) A model for the prediction of lattice parameters of iron–carbon austenite and martensite. J Alloy Compd 420(1–2):117–120
17. Zhang M-X, Kelly P, Bekessy L, Gates J (2000) Determination of retained austenite using an X-ray texture goniometer. Mater Charact 45(1):39–49
18. Luzginova N, Zhao L, Sietsma J (2007) Evolution and thermal stability of retained austenite in SAE 52100 bainitic steel. Mater Sci Eng A 448(1):104–110
19. Erdos E (1983) Analysis of high temperature materials, vol 204. Applied Science Publishers, London
20. Franck FJ, Tambuyser P, Zubani I (1982) X-ray powder diffraction evidence for the incorporation of W and Mo into $M_{23}C_6$ extracted from high-temperature alloys. J Mater Sci 17(10):3057–3065
21. Isfahany AN, Saghafian H, Borhani G (2011) The effect of heat treatment on mechanical properties and corrosion behavior of AISI420 martensitic stainless steel. J Alloy Compd 509(9):3931–3936
22. Candelária AF, Pinedo CE (2003) Influence of the heat treatment on the corrosion resistance of the martensitic stainless steel type AISI 420. J Mater Sci Lett 22(16):1151–1153
23. Hippenstiel F, Lubich V, Vetter P, Grimm W (2004) Handbook of Plastics Mould Steels. Edelstahlwerke Buderus AG, Wetzlar
24. Shtansky D, Inden G (1997) Phase transformation in Fe-Mo-C and Fe-WC steels: II. Eutectoid reaction of $M_{23}C_6$ carbide decomposition during austenitization. Acta Mater 45(7):2879–2895
25. Hong H, Rho B, Nam S (2001) Correlation of the $M_{23}C_6$ precipitation morphology with grain boundary characteristics in austenitic stainless steel. Mater Sci Eng A 318(1):285–292
26. Tang B, Jiang L, Hu R, Li Q (2013) Correlation between grain boundary misorientation and $M_{23}C_6$ precipitation behaviors in a wrought Ni-based superalloy. Mater Charact 78:144–150
27. Dong ZH, Shi W, Guo XP (2011) Initiation and repassivation of pitting corrosion of carbon steel in carbonated concrete pore solution. Corros Sci 53(4):1322–1330
28. Lorang G, Belo MDC, Simoes AMP, Ferreira MGS (1994) Chemical composition of passive films on AISI 304 stainless steel. J Electrochem Soc 141(12):3347–3356

29. Marcelin S, Pébère N, Régnier S (2013) Electrochemical characterisation of a martensitic stainless steel in a neutral chloride solution. Electrochim Acta 87:32–40

30. He H, Zhang T, Zhao C, Hou K, Meng G, Shao Y, Wang F (2009) Effect of alternating voltage passivation on the corrosion resistance of duplex stainless steel. J Appl Electrochem 39(5):737–745

31. El-Egamy S, Badaway W (2004) Passivity and passivity breakdown of 304 stainless steel in alkaline sodium sulphate solutions. J Appl Electrochem 34(11):1153–1158

32. Hirschorn B, Orazem ME, Tribollet B, Vivier V, Frateur I, Musiani M (2010) Determination of effective capacitance and film thickness from constant-phase-element parameters. Electrochim Acta 55(21):6218–6227

33. Dong ZH, Zhu T, Shi W, Guo XP (2011) Inhibition of ethyleneamine on the pitting corrosion of rebar in a synthetic carbonated concrete pore solution. Acta Phys Chim Sin 27:905–912

34. Candelaria A, Pinedo C (2003) Influence of the heat treatment on the corrosion resistance of the martensitic stainless steel type AISI 420. J Mater Sci Lett 22(16):1151–1153

35. Hill H, Huth S, Weber S, Theisen W (2011) Corrosion properties of a plastic mould steel with special focus on the processing route. Mater Corros 62(5):436–443

36. Zhang L, Zhang W, Jiang Y, Deng B, Sun D, Li J (2009) Influence of annealing treatment on the corrosion resistance of lean duplex stainless steel 2101. Electrochim Acta 54(23):5387–5392

37. Guo LQ, Lin MC, Qiao LJ, Volinsky AA (2013) Ferrite and austenite phase identification in duplex stainless steel using SPM techniques. Appl Surf Sci 287:499–501